RESEARCH PAPER

PCCP
www.rsc.org/pccp

Bubble guidance of tubular growth in reaction–precipitation systems

Stephanie Thouvenel-Romans, Jason J. Pagano and Oliver Steinbock*

Department of Chemistry and Biochemistry, Florida State University, Tallahassee, FL 32306-4390, USA. E-mail: steinbck@chem.fsu.edu; Fax: +1 850 644 8281; Tel: +1 850 644 4824

Received 30th March 2005, Accepted 6th May 2005
First published as an Advance Article on the web 1st June 2005

Numerous types of reaction–precipitation systems involve the growth of tubular structures similar to those formed in "silica gardens". As a model case for this phenomenon, we investigate the rapid growth of hollow tubes in the reaction between sodium silicate and cupric sulfate. The latter solution is injected hydrodynamically at constant flow rates of 1–20 mL h^{-1} into a large reservoir of waterglass. In this study, the growth is templated and guided by single, buoyant gas bubbles. The resulting tubes can be several decimetres long and have constant radii in the range of 100–600 μm. Systematic measurements show that bubble size governs the tube radius. According to this radius, the system selects its growth velocity following volume conservation of the injected solution. Moreover, scanning electron microscopy reveals intricate ring patterns on the tube walls. We also show evidence for the existence of a minimal and a maximal tube radius. Finally, we report an intriguing collapse of tubes created at high silicate concentrations, which yields twisted ribbon-like structures. Critical radii and tube collapse are discussed in terms of simple competing forces.

Introduction

Self-organization in reaction–precipitation systems often leads to the formation of permanent tubular structures. Some of the most striking ones are 30 m high, black "smokers" growing at hydrothermal vents on the ocean's floor.[1] As hot acidic, mineral-rich water from below the earth's crust surges into the cool, alkaline ocean the dissolved minerals precipitate and aggregate in a ring-shape area at the jet's boundary. Another geological example, soda-straw stalactites result from the periodic detachment of calcium carbonate-saturated water droplets in caves.[2,3] The pH increases during the drops' hang-time and precipitation of $CaCO_3$ occurs at the rim. This rhythmic deposition of material creates meter-long tubes of small but constant diameter. Similarly, capillary forces can create helictites, gravity defying structures, which grow along curved, spiral-like paths.[4] On a microscopic scale, hollow fibers form in setting Portland cement[5,6] as well as in certain corrosion systems.[7–9] More recently, Goldstein *et al.* studied "ferrotubes" in an electrochemical system. In their experiment, small tubes are templated by successive detachment of gas bubbles formed at a steel cathode.[10]

All of these phenomena share similarities with precipitation tubes in chemical (or silica) gardens which can be considered a prototypic case of gradient-induced tube formation in reaction–precipitation systems. Descriptions of the latter system are found as early as the 17th century.[11,12] Today, chemical gardens are known to many as a demonstration experiment that readily creates colorful, plant-like precipitation structures. Their formation is observed for many inorganic salts (*e.g.*, $CuSO_4$, $MnCl_2$, $FeCl_3$), crystals of which are placed into concentrated solutions containing anions such as silicate, phosphate or borate. Moreover, recent investigations of the properties of the material synthesized have contributed to a renewed scientific interest in chemical gardens. For example, Collins *et al.* reported evidence of surprisingly strong catalytic activity and discovered hierarchical nano- to micrometre structures in overall amorphous aluminosilicate precipitates.[13,14]

Fig. 1 shows a typical landscape generated from cupric nitrate crystals seeded into 1 M silicate solution (waterglass). The surface of the seeds dissolves and reacts to form an insoluble metal hydroxide membrane. As the concentration of metal ion increases, osmotic pressure builds up and inflow of water across the membrane causes it to yield and rupture. The resulting release of buoyant solution into the surrounding waterglass creates hollow, vertical structures (see left-hand side of Fig. 1). Their initiation and growth occurs in a matter of seconds to days depending on the salts employed.

In some instances, small air bubbles are attached to the surface of the colloidal membrane.[15,16] The detachment and rise of a bubble entrains the inner solution in its wake, thus, directing the rapid growth of a thin, hollow needle. Several examples of tubes formed in this fashion are seen in Fig. 1. A magnified view of a bubble still attached to the stalk is shown in the inset. The variation in the diameter and length of the needle-like structures is related to the size of the bubble drawing the inner solution along. Large bubbles moving along straight trajectories create wide precipitation tubes that taper as the supply of solution is depleted. More erratic paths are sometimes observed for thin tubes created by smaller bubbles.

Here, we present a systematic investigation of bubble-guided tube growth. To allow quantitative variations of relevant control parameters, we have modified a recent method developed by Thouvenel-Romans *et al.*[17,18] In both cases, the seed crystals are replaced by a seed solution which is injected hydrodynamically at well-defined flow rates and concentrations.

Experimental

Synthesis

A solution of 0.5 M cupric sulfate ($CuSO_4 \cdot 5H_2O$; Fisher) is injected into sodium silicate solutions ($Na_2SiO_3 \cdot 5H_2O$; Fisher) of various concentrations at 25 ± 1 °C. All solutions are prepared using nano-pure water (18 MΩ cm; EASYpure® UV, Barnstead). The injection rate of the aqueous cupric

DOI: 10.1039/b504407c

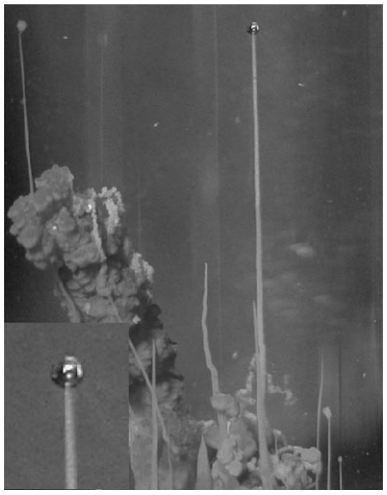

Fig. 1 Typical example of tubular growth from $Cu(NO_3)_2$ crystals seeded into 1 M sodium silicate solution. The inset shows a magnified view of an air bubble attached to the end of a needle-like precipitation structure. Field of view: 1.9 × 2.5 cm^2; inset: 2.4 × 3.2 mm^2.

sulfate solution is controlled by a syringe pump (KD Scientific 200) and varied between 1–20 mL h^{-1}. A glass capillary (length = 15 mm; inner diameter ≈ 1.1 mm) is used as a nozzle and delivers the cupric sulfate solution into a large, waterglass-filled cylinder (height ≈ 28 cm, inner diameter = 2.2 cm). A stainless steel needle (23G, Bevel B-D Yale) is introduced into the capillary with its tip slightly protruding out. The needle is connected to an air-filled syringe used to manually inject single air bubbles into the flow of cupric sulfate solution. Each bubble entrains the buoyant solution upward, forming a single tube of precipitate in its wake. Optical micrographs of the growth are acquired with a monochrome charged-coupled device camera (COHU 2122) connected to a PC *via* a frame grabber board (Data Translation, 640 × 480 pixels at 8 bit $pixel^{-1}$). During the experiment, image sequences are captured using HLImage++97 software at a rate of typically 10 frame s^{-1}. The images are then analyzed using in-house software. All measurements are corrected for optical deformations caused by the cylindrical geometry of the main reaction vessel.

Microscopy

Samples are synthesized at a pump rate of $Q = 7$ mL h^{-1} using $[CuSO_4] = 0.5$ M and $[Na_2SiO_3] = 1.0$ M. Collapsed tubes are produced at Q = 10–15 mL h^{-1} using $[CuSO_4] = 0.5$ M and $[Na_2SiO_3] = 2.5$ M. The tubes generated are collected in a Petri dish filled with nano-pure water. The pieces of the tube are then rinsed three times and excess water is removed. The samples are dried at 45 °C overnight. Higher temperatures induce the degradation of the copper hydroxide precipitate to black copper oxide. The specimens are placed in a vacuum desiccator to remove remaining moisture. Then, they are either carbon coated or gold sputtered prior to acquiring micrographs using a JEOL JSM-5900 scanning electron microscope (SEM).

Results and discussion

In a recent publication, two of us have reported that the injection of cupric sulfate solution into sodium silicate solution leads to the formation of tubular structures. Three different growth regimes are distinguished.[17]

(1) Jetting growth: At low concentrations of cupric sulfate solution, hydrodynamics dominates the formation of precipitation tubes by templating the membrane at the interface between the jetting fluid and the outer, denser liquid. The tube radii are described quantitatively by the Poiseuille-flow characteristics of the buoyant jet of injected solution.[18]

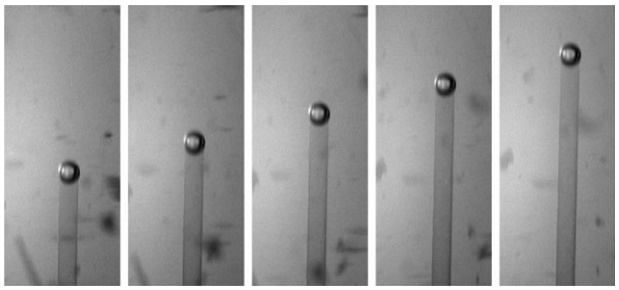

Fig. 2 Image sequence of an air bubble (R_{bubble} = 310 μm) directing the growth of a precipitation tube (r_{tube} = 240 μm) in 1.0 M sodium silicate solution. In this experiment, cupric sulfate solution (0.5 M) is injected at a constant flow rate of 3.0 mL h^{-1}. The structure grows upward at a speed of 0.38 cm s^{-1}. Time lapse between frames: 200 ms; field of view: 3.0 × 7.3 mm^2.

(2) Popping growth: At intermediate concentrations, tubes grow in an oscillatory fashion. The tip of the tube is sealed by a colloidal membrane which stretches into a buoyant, membrane-bound droplet as solution delivery continues. When the material ruptures, this small solution-filled envelop is released and rises to the surface. This sequence repeats continuously with oscillation periods of approximately 1–12 s causing tube growth at speeds of 0.05–0.35 mm s^{-1}.

(3) Budding growth: For high concentrations of cupric sulfate, buoyancy forces are not large enough to remove the membrane-bound droplet from its hollow stalk. New growth appears through random breaches on the freshly formed membrane without ejection of material. Nonetheless, budding growth tends to be periodic yielding bulging but unbranched, hollow structures.

Under budding conditions, the introduction of an air bubble at the interface between the two reactants emulates the bubble-guided growth shown in Fig. 1. As the bubble detaches from the syringe tip, it is released into the reaction zone between the two fluids and the air is trapped by a very thin colloidal copper hydroxide membrane. The buoyancy of the gas directs the growth upward. Fig. 2 shows an image sequence of a bubble rising in 1.0 M sodium silicate solution. In its wake, an initially translucent tube is rapidly forming. The bubble travels upward but remains anchored to the mouth of the structure. Sometimes, however, the bubble detaches and the system switches to its natural growth regime. We note that the gradual change between the upper translucent zone and the non-transparent blue stalk corresponds to fast formation of colloidal copper hydroxide and slower silica precipitation, respectively. This is in agreement with preliminary results from micro-Raman and EDS studies of the tube material, which detect predominantly copper hydroxide on the interior of the wall surface and amorphous silica on the outside.

Our experiments show that the growth velocity of a tube is remarkably constant. This observation is exemplified by the data shown in Fig. 3 where the vertical coordinate h of three bubbles is plotted as a function of time. The bubbles' velocities are obviously identical to the growth velocity of the tubes but smaller than the terminal velocity of free-rising bubbles. Notice that the height increases linearly over 4 to 6 cm which is approximately 100 times larger than the bubble and tube diameters. The origin $h = 0$ in the graph is situated 2 cm from the capillary outlet. At closer distances, transient fluctuations occur that are caused by momentum imparted to the bubble during its release. Moreover, as the bubble reaches the last few centimeters below the silicate solution/air interface, the growth velocity is no longer constant but increases rapidly and the radius of the tube decreases noticeably. This acceleration is possibly caused by a gradient in fluid viscosity close to the meniscus of the silicate solution and/or the effects of the interface on the flow field.

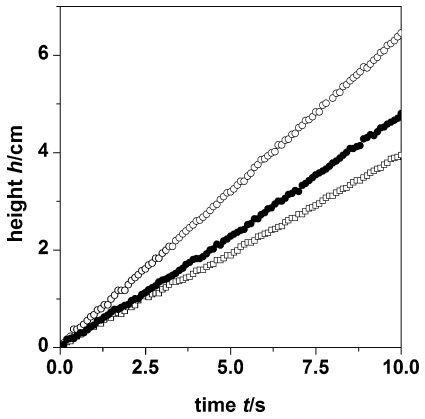

Fig. 3 Height evolution of growing tubes for three different experimental conditions (○ 10 mL h^{-1}, $[Na_2SiO_3] = 2.0$ M; ● 5 mL h^{-1}, $[Na_2SiO_3] = 1.5$ M; □ 3 mL h^{-1}, $[Na_2SiO_3] = 1.5$ M). The growth velocities are 0.64, 0.48, 0.40 cm s^{-1}, respectively. All experiments are carried out with $[CuSO_4] = 0.5$ M at 25 °C.

Systematic measurements are carried out to obtain insights into the dependencies of the growth velocity v and the tube radius r_{tube} on the injection rate Q and the bubble radius R_{bubble}. A key question is whether the injected solution remains within the growing tube or leaks into the surrounding liquid without contributing to the volume increase of the structure. In the absence of such leaks, the flow rate Q should equal the tube's rate of volume change. This yields the simple equation $v = Q/\pi r_{tube}^2$. Fig. 4 compares this relation with experimental data obtained for flow rates between 2 mL h^{-1} (solid triangles) and 10.0 mL h^{-1} (solid squares), and various bubble sizes. We find an overall good agreement between the experimental data and the latter equation (see solid lines in Fig. 5A,B). Least-

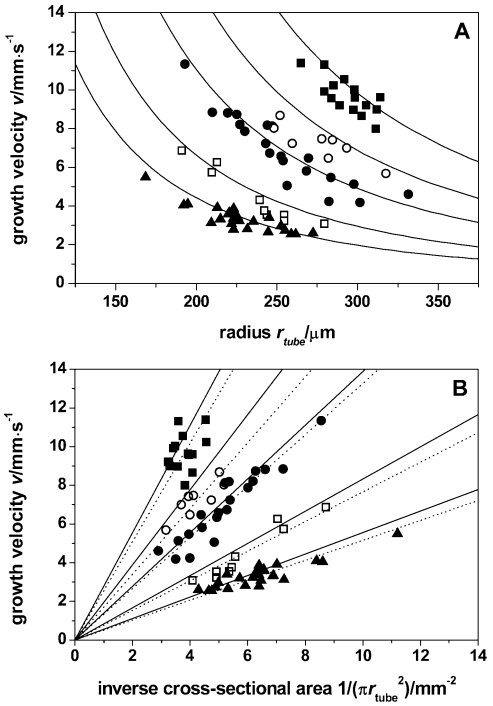

Fig. 4 (A) Tube growth velocity as a function of tube radius. The cupric sulfate and sodium silicate concentrations are kept constant at 0.5 M and 1.0 M, respectively. The cupric sulfate solution is delivered with a syringe pump at five different flow rates (■ 10.0 mL h^{-1}, ○ 7.0 mL h^{-1}, ● 5.0 mL h^{-1}, □ 3.0 mL h^{-1}, ▲ 2.0 mL h^{-1}). The solid curves represent the dependencies expected under the assumption of volume conservation ($v = Q/\pi r_{tube}^2$). (B) The same data are plotted as a function of the tubes' inverse cross-sectional area. Dotted lines are fits assuming proportionality. Solid lines represent $v = Q/\pi r_{tube}^2$ with Q denoting the pump rates employed.

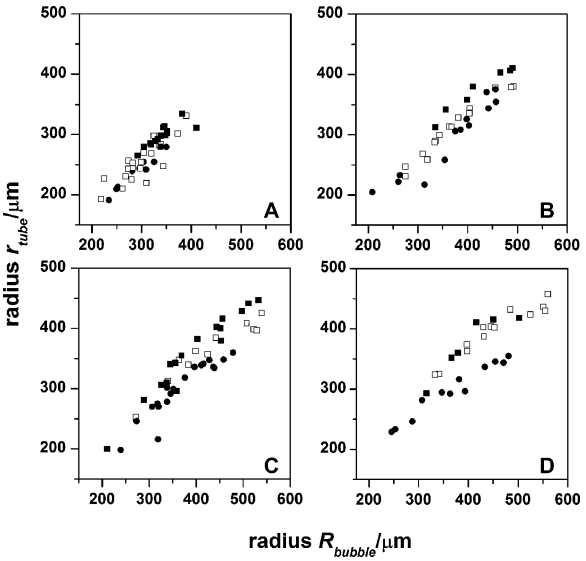

Fig. 5 (A) through (D) correspond to plots of the tube radius as a function of bubble radius for waterglass concentration of 1.0 M, 1.5 M, 2.0 M, and 2.5 M, respectively. All experiments involve the injection of 0.5 M cupric sulfate solution. Three different flow rates Q are used (● 3 mL h^{-1}, □ 5 mL h^{-1}, ■ 10 mL h^{-1})

square fitting of the data (see dashed lines in Fig. 4B) yields observed flow rates that are about 8% smaller than the pump rates employed (−7.0%, −8.0%, −4.4%, −12.5% and −8.3% for $Q = 2.0$, 3.0, 5.0, 7.0, and 10.0 mL h^{-1}, respectively). These relatively small deviations indicate that most of the injected solution stays within the growing tube. Consequently, the formation of new membrane material is sufficiently fast to avoid significant leakage. Under our experimental conditions, the rate-determining factor of tube growth is therefore the inflow of seed solution and not the kinetics of membrane formation.

Visual inspection readily shows that tube growth occurs in close vicinity to the bubble rather than at the tube's base. We characterize this crucial reaction zone by measuring the radii of both the bubble and the tube that forms in its trail. In this context, it is important to note that, within the resolution of our experiments, all bubbles had a simple spherical shape. Fig. 5A–D show the tube radii as a function of bubble size for four different silicate concentrations. Each plot presents data from experiments at flow rates of $Q = 3$, 5, 10 mL h^{-1} as solid circles, open squares and solid squares, respectively. For each data set, we find a nearly proportional dependence of r_{tube} on R_{bubble}. We will therefore continue our discussion in terms of the corresponding radii ratio.

Fig. 6 shows this ratio for four different silicate concentrations and three different flow rates. The concentration of cupric sulfate is kept constant at 0.5 M. We note that the radii ratio has a simple geometrical interpretation as it corresponds to the angle α between the boundary of the tube and the bubble surface ($\cos\alpha = r_{tube}/R_{bubble}$); hence, the smaller the angle, the deeper the bubble sits in the mouth of the tube. Examples of small and large angles are shown in the left and right inset of Fig. 6, respectively. The data span the entire range of silicate concentrations (1.0–2.5 M) for which the bubbles are consistently creating simple tubes. Below 1.0 M, the membrane is tenuous and it is difficult to generate a bubble that drags the copper solution upward. Silicate concentrations above 2.5 M yield collapsing tubes.

Fig. 6 shows that tube radii are only 5–20% smaller than the radii of their guiding bubbles. Within this range, the smallest ratios are found for the lowest flow rate of $Q = 3$ mL h^{-1}. At this value, no significant dependence on silicate concentration is found. For $Q = 10$ mL h^{-1}, however, the ratio increases with increasing silicate concentration and the contact angle

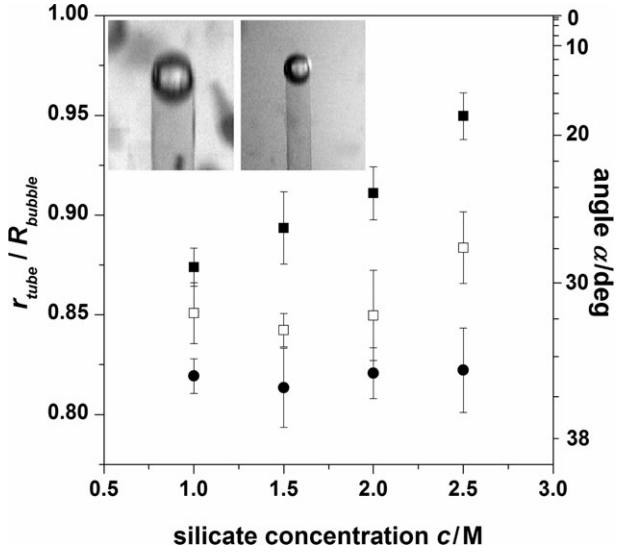

Fig. 6 Average radii ratio for three different flow rates Q (■ 10 mL h^{-1}, □ 5 mL h^{-1}, ● 3 mL h^{-1}). All experiments involve the injection of 0.5 M cupric sulfate solution. The left and right insets show examples of a small contact angle (20°) ($[Na_2SiO_3] = 2.5$ M, $Q = 10$ mL h^{-1}) and a large contact angle (36°) ($[Na_2SiO_3] = 1.0$ M, $Q = 3$ mL h^{-1}), respectively. Field of view of both insets: 2.5 × 3.0 mm^2.

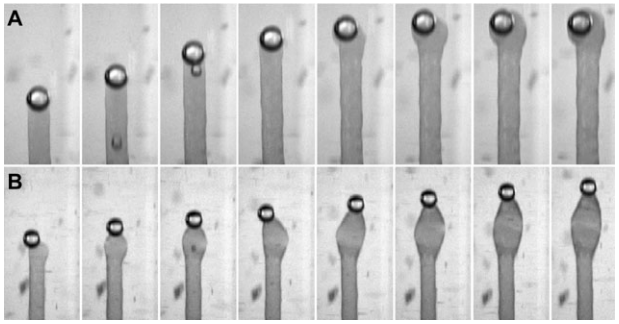

Fig. 7 Failure of bubble guidance. (A) A smaller bubble is injected into the growing structure, rises up the tube interior and fuses with the leading bubble. Subsequently, the fused bubble is incorporated into the tube. Time between frames: 200 ms, $[Na_2SiO_3] = 2.0$ M, $[CuSO_4] = 0.5$ M, $Q = 10$ mL h^{-1}, field of view: 3.1 × 6.5 mm^2. (B) Spontaneous descent of the reaction zone away from the bubble. This failure of the gas bubble to pull the forming membrane results in a transition to the popping regime. Time between frames: 200 ms, $[Na_2SiO_3] = 2.5$ M, $[CuSO_4] = 0.5$ M, $Q = 3$ mL h^{-1}, field of view: 3.1 × 6.6 mm^2.

decreases accordingly from about 30° to 20°. Moreover, we find that for a given silicate concentration, the radii ratio increases with increasing flow rate. This dependence is most pronounced for the highest silicate concentration (2.5 M).

Our experiments also show that only bubbles of certain sizes are capable of guiding tubular growth. We only succeeded in creating tubes for bubbles with radii in the range of 150–600 μm. Moreover, our experiments suggest that, with increasing flow rate, the minimal and maximal radii shift to larger values. Since the tube and the bubble radii are closely related, as we discussed in the earlier paragraphs, this trend is also reflected by the range of the data in Fig. 4.

The existence of a minimal and a maximal radius can be qualitatively argued in the context of competing forces. The buoyancy acting on the air bubble scales as R_{bubble}^3. Two forces are counteracting buoyancy, namely a "sticking" force due to the contact between the membrane and the gas bubble and the Stokes force due to the viscosity of the silicate solution around the growing, bubble-guided tube. The Stokes force is proportional to $\eta_o R_{bubble} v = \eta_o R_{bubble} Q/(\pi r_{tube}^2)$ where η_o denotes the viscosity of the silicate solution. Therefore, this force roughly scales as $1/R_{bubble}$ while the sticking force is likely to scale as R_{bubble}. Accordingly, the buoyancy of very large bubbles is greater than the combined contributions from "sticking" and Stokes forces and the bubble detaches. For very small bubbles, the Stokes force is dominant and the bubble cannot act as a sufficiently strong guide for the growing tube. While this discussion motivates the existence of a finite range of radii in bubble-guided tube growth, more insights into the nature of the sticking force are needed. We also note that the size, the shape and the position of the injection needle might affect measurements of minimal and maximal radii.

The delicate force balance needed for bubble-guided tube growth can be easily upset. In Fig. 7A, a second smaller air bubble is injected deliberately into the growing tube. This bubble rises up the hollow tube and eventually collides with the leading bubble. When the two coalesce, the force balance is disturbed and the bubble is engulfed by the colloidal membrane. As more copper solution is delivered by the pump, the system transitions to its natural growth regime (budding) and the tube widens into the expected bulging structure. The bubble has lost its ability to guide the tube's growth.

An example of a different outcome is shown in Fig. 7B. Here, the zone underneath the bubble begins to inflate, thus, stretching the sides of the tube. Nonetheless, the bubble is still attached to the top of the tube while the inflow of solution moves it from side to side. The lighter shades of gray at the thickest part of the bulge indicate thinning of the membrane or some newly produced material. It appears that in this case the growth zone moved away from the bubble, thus, rendering the guide ineffective. For the conditions of this particular experiment, the resulting structure is growing in the popping regime and, consequently, the top portion of the stalk and the attached bubble are released shortly after the time of the last snapshot.

Additional features of bubble-guided tube growth are unveiled by examining the tubes' micrometre-scale features. We investigate the morphology of the tube walls using scanning electron microscopy. Samples are prepared according to the procedures described in the experimental section. Fig. 8A shows a typical tubular structure attached to the dark background of a carbon tape. In this example, the tube radius is approximately 250 μm. The micrograph reveals stripes of different texture along the tube. For the given experimental parameters, the wavelength of the stripe pattern varies between 200 μm and 250 μm. We emphasize that these stripe patterns are also discernible on the inside surface as we observed numerous times during SEM studies of broken tube segments.

At higher magnification (Fig. 8B), we can clearly discern two distinct surface textures that alternate within this stripe pattern. One appears dark and smooth (see upper left-hand corner of Fig. 8B) while the other one is lighter with a coarse, grainy appearance (lower right-hand corner). Additional features include blister-like structures (typical diameter 50 μm), most of which flank the transition regions within the stripe pattern.

One can envision a variety of different mechanisms that may cause the observed stripe patterns on bubble-guided tubes. These include oscillatory phenomena within or around the primary reaction zone (*e.g.*, periodic rupturing of the freshly formed membrane material), Liesegang-like processes that influence the relevant precipitation reactions, and shape oscillations of the guiding gas bubble. Any oscillatory mechanism acting during the growth process corresponds to a characteristic frequency that can be calculated from the growth velocity of the tube and the wavelength of the stripe pattern. For the example shown in Fig. 8, the growth speed of 1.0 cm s^{-1} and the stripe distance of about 250 μm correspond to a frequency of approximately 40 Hz. Inspection of several other samples yields frequencies in the range of 30–90 Hz. However, further interpretations require more systematic measurements and a thorough characterization of compositional variations throughout the striped wall material.

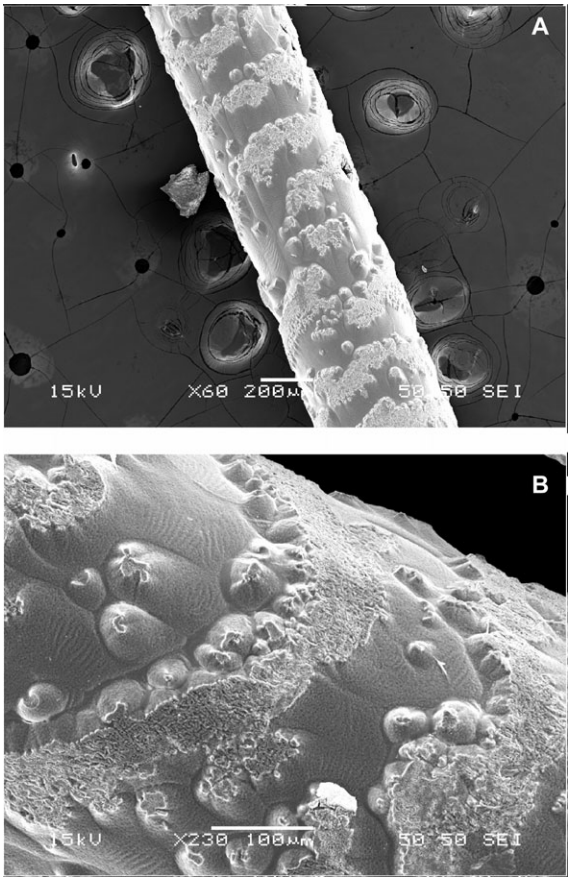

Fig. 8 Scanning electron micrographs of a carbon-coated tube. (A) The surface shows periodic stripes with a spacing of approximately 200–250 μm. (B) At higher magnification the stripes reveal intricate surface features. Experimental parameters: $Q = 7$ mL h^{-1}, [$CuSO_4$] = 0.5 M, [Na_2SiO_3] = 1.0 M.

Another intriguing phenomenon is observed for high silicate concentrations (≥ 2.5 M), which correspond to large density differences between the dense silicate and the lighter cupric sulfate solution. Under these experimental conditions, we observe that the bubble-guided tubes collapse. This process yields twisted ribbon-like structures. A typical example for these collapsed tubes is shown in Fig. 9A. The ribbon is approximately 1.5 mm wide and has five well-defined twists within the field of view. Accordingly, the structure has a pitch of about 6 mm.

Fig. 9B and 9C show scanning electron micrographs of a collapsed tube. The overall morphology of the sample is more rugged than in the case of the uncollapsed structures (*cf.*, Fig. 8). Also the characteristic stripe pattern appears to be absent although very coarse ring-like ridges are found. The outer wall surfaces of the collapsed tube also reveals numerous blisters and the twist is easily discernible as a large fold. Some of the barnacle-like blisters feature little spirals such as the very left one in Fig. 9C.

Tube collapse occurs after several centimetres of ordinary, cylindrical growth, but our experiments did not reveal a well-defined critical length. Typically the structure flattens and twists nearly simultaneously with the entire collapse requiring only a few seconds. In the following, the bubble-guided growth process continues but the resulting precipitation structure forms as a twisted ribbon. This observation reveals that the collapsed state still allows internal flow of solution. We also observed that stopping and restarting of the pump can induce a transition back to the cylindrical or a near cylindrical state. This phenomenon of "re-inflation" indicates that the growth of the collapsed structure is actually cylindrical in close vicinity of the bubble.

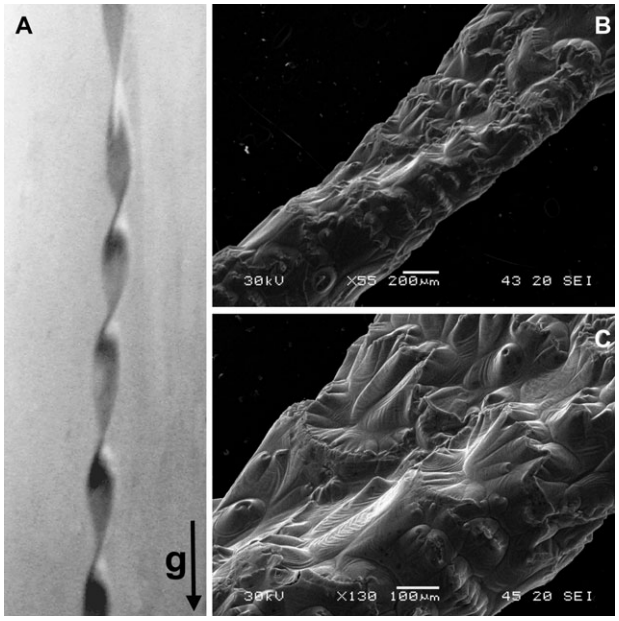

Fig. 9 (A) Optical micrograph of a collapsed tube produced by injecting 0.5 M cupric sulfate solution into 2.5 M silicate solution at a flow rate of $Q = 10$ mL h^{-1}. As the leading bubble rises in the outer solution, the tube starts to flatten and twist. Field of view: 3.0 × 1.0 cm^2. (B,C) Scanning electron micrographs of a gold sputtered, twisted tube at two different magnifications. This sample was obtained at $Q = 15$ mL h^{-1}, [$CuSO_4$] = 0.5 M, and [Na_2SiO_3] = 2.5 M.

The collapse of precipitation tubes is obviously related to an increased density difference $\Delta\rho = \rho_o - \rho_i$ between the outer silicate ('o') and the inner cupric sulfate solution ('i'). Assuming mechanical equilibrium at the top of the growing tube, one obtains the hydrostatic pressure difference $\Delta p = \Delta\rho g h$ across the membrane, where g and h denote earth's acceleration and the vertical distance from the growth zone, respectively. This transmural pressure difference exerts a compressive force on the cylindrical tube. In the actual growth experiment, flow within the structure contributes an opposing pressure that follows the Hagen-Poiseuille equation $\Delta p = (8\eta_i h Q)/(\pi r_{tube}^4)$ where η_i is the viscosity of the cupric sulfate solution. If one further assumes that the freshly formed wall does not resist a possible collapse, one obtains the simple stability criterion $(8\eta_i Q)/(\pi\Delta\rho g r_{tube}^4) > 1$. We therefore expect that collapse occurs for low flow rates, large density differences and large radii. This conclusion is in qualitative agreement with the observation that structures grown at $Q = 10$ mL h^{-1} are stable if the tube radii are less than approximately 450 μm whereas wider tubes collapse. However, the predicted critical radius for $Q = 10$ mL h^{-1}, $\eta_i = 1.21$ cP, and $\Delta\rho = 0.2$ g cm^{-3} is 250 μm and, hence, smaller than the observed value. This difference could be the result of a certain rigidity of the tube material and/or indicate a small but non-zero pressure difference between the inner and outer solutions at the reaction zone.

While our qualitative discussion motivates some of the dependencies relating to tube collapse, it does not explain the occurrence of the striking helical twist that accompanies the flattening of the structure. However, this feature is observed for nearly all collapsing tubes. We suggest that the twisting motion is a secondary aspect of the collapse that reflects the mechanical characteristics of the tube material; in particular, its gradient-like vertical and radial composition as well as the specific boundary conditions that immobilize the lower end while allowing unconstrained motion of the upper extremity.

Conclusions

In summary, this study provides the first quantitative insights into the rapid growth dynamics of tubular precipitation

structures guided by buoyant gas bubbles. The tube radii are controlled primarily by the radius of the rising bubble. Based on this simple radius selection, the system determines its growth velocity following volume conservation of the injected reactant solution. Moreover, cylindrical tubes collapse to helical ribbons if the density difference across the tube wall is large enough to cause compressive pressure that outbalances flow-induced and other stabilizing forces.

A key question that remains unanswered concerns the nature of the adhesive contact between the gas bubble and the forming copper hydroxide membrane at the tip of the tube. Failure to establish or maintain a proper contact results in slow tubular growth that is not templated by the bubble. Our experiments suggest that such a situation occurs outside of a finite range of bubble radii. In particular, large bubbles are lifted out of the reaction zone due to their pronounced buoyancy. This process appears to be related to the pinning of bubbles to solid walls or interfaces between immiscible liquids. In our experiments, however, this situation is complicated by the unknown flow and concentration fields around the upper portion of the growing structure. Nonetheless, it appears likely that bubbles stick to the reaction zone due to surface tension. Consequently, more detailed measurements of the upper, critical radius might allow the characterization of transient surface tensions. Such measurements could provide useful data concerning the early stages of the formation of colloidal membranes.

Our findings are of additional importance as they relate to a wide class of precipitation systems in which radial gradient fields orchestrate the formation of permanent, tubular structures. As described in the Introduction, these systems span through a diverse range of fields including electrochemistry, materials science, geology and also biomineralization.[19,20] Our investigation is the first step towards the development of methodologies that will allow us to template, guide, and control the formation of precipitation structures in diverse systems. Such approaches not only will reveal underlying universalities but could potentially lead to novel materials and devices.

Acknowledgements

This work was supported by the National Science Foundation and the American Chemical Society Petroleum Research Fund. Scanning electron microscopy was carried out at Florida State University's Center for Materials Research and Technology (MARTECH). We thank Tedric Campbell for technical assistance.

References

1 J. B. Corliss, J. Dymond, L. I. Gordon, J. M. Edmond, R. P. Von Herzen, R. D. Ballard, K. Green, D. Williams, A. Bainbridge, K. Crane and Tj. H. van Andel, *Science*, 1979, **293**, 1073.
2 W. B. White, in *Cave Minerals and Speleothems. The Science of Speleology*, ed. T. D. Ford and C. H. D. Cullingford, Academic Press, London, 1976, p. 267.
3 M. B. Short, J. C. Baygents, J. W. Beck, D. A. Stone, R. S. Toomey III and R. E. Goldstein, *Phys. Rev. Lett.*, 2005, **94**, 18501.
4 L. C. Huff, *J. Geol.*, 1940, **48**, 641.
5 D. D. Double, A. Hellawell and S. J. Perry, *Proc. R. Soc. London, Ser. A*, 1978, **359**, 435.
6 D. Balköse, F. Özkan, U. Köktürk, S. Ulutan, S. Ülkü and G. Nişli, *J. Sol-Gel Sci. Technol.*, 2002, **23**, 253.
7 A. Ackermann, *Kolloid Z.*, 1932, **59**, 49.
8 M. G. Fontana, *Corrosion Engineering*, McGraw-Hill, New York, 1986.
9 R. D. Coatman, N. L. Thomas and D. D. Double, *J. Mater. Sci.*, 1980, **15**, 2017.
10 D. A. Stone and R. E. Goldstein, *Proc. Natl. Acad. Sci. USA*, 2004, **101**, 11537.
11 J. R. Glauber, *Furni Novi Philosophici*, Amsterdam, 1646.
12 J. Keir, *Philos. Trans., R. Soc. London*, 1790, **80**, 359.
13 C. Collins, R. Mokaya and J. Klinowski, *Phys. Chem. Chem. Phys.*, 1999, **1**, 4669.
14 C. Collins, G. Mann, E. Hoppe, T. Duggal, T. L. Barr and J. Klinowski, *Phys. Chem. Chem. Phys.*, 1999, **1**, 3685.
15 T. H. Hazlehurst, *J. Chem. Educ.*, 1941, **18**, 286.
16 J. H. E. Cartwright, J. M. Garciá-Ruiz, M. L. Novella and F. Otálora, *J. Colloid Interface Sci.*, 2002, **256**, 351.
17 S. Thouvenel-Romans and O. Steinbock, *J. Am. Chem. Soc.*, 2003, **125**, 4338.
18 S. Thouvenel-Romans, W. van Saarloos and O. Steinbock, *Europhys. Lett.*, 2004, **67**, 42.
19 S. Mann, *Biomineralization: Principles and Concepts in Bioinorganic Materials Chemistry*, Oxford University Press, Oxford, 2001.
20 J. M. Garciá-Ruiz, S. T. Hyde, A. M. Carnerup, A. G. Christy, M. J. Van Kranendonk and N. J. Welham, *Science*, 2003, **302**, 1194.